

Liquid-like to gas-like dynamical crossover in supercritical water

Peihao Sun* and Jerome B. Hastings

SLAC National Accelerator Laboratory, 2575 Sand Hill Rd, Menlo Park, CA 94025, USA

Daisuke Ishikawa and Alfred Q. R. Baron

Materials Dynamics Laboratory, RIKEN SPring-8 Center, 1-1-1 Kouto, Sayo, Hyogo 679-5148, Japan

Giulio Monaco

Dipartimento di Fisica, Università di Trento, I-38123 Povo (Trento), Italy

(Dated: July 29, 2022)

Molecular-scale dynamics in sub- to super-critical water is studied with inelastic X-ray scattering and molecular dynamics simulations. The obtained longitudinal current correlation spectra can be decomposed into two main components: a low-frequency (LF), gas-like component and a high-frequency (HF) component arising from the O–O stretching mode between hydrogen-bonded molecules, reminiscent of the longitudinal acoustic mode in water under ambient conditions. With increasing temperature, the hydrogen-bond network diminishes and the spectral weight shifts from HF to LF, leading to a transition from liquid-like to gas-like dynamics with rapid changes around the Widom line. The changing ratio between the components is used to explain the thermodynamic state dependence of physicochemical properties of supercritical water such as its dielectric constant.

The supercritical state of water was discovered almost 200 years ago [1], but there were few subsequent studies for a long time due to experimental challenges. In recent years, however, interest in supercritical water has been growing. This is not only because of its natural occurrence around hydrothermal vents [2, 3] and in the Earth’s mantle [4] which are of biological and geological importance, respectively, but also because of its wide application in bio-chemical technologies such as green materials synthesis [5], biofuel production [6], and industrial waste treatment [7]. Underlying many of these applications is the large tunability of density and solvation properties near the critical point [6, 8]. For water in particular, as temperature increases in the near-critical region, its solubility for inorganic ionic compounds decreases rapidly, while many simple organic compounds and gases become soluble or even completely miscible in supercritical water [6]. These properties have been and may be further exploited to facilitate a variety of chemical processes in supercritical water [6, 9].

From a physical viewpoint, supercritical fluids have attracted attention recently because evidence suggests the existence of “liquid-like” and “gas-like” states beyond the critical point [10, 11]. A number of recent studies have thus focused on the transition between the two; in particular, the “Widom line” (WL), defined as the line of maximum correlation length in the supercritical region [12], has been proposed as a liquid/gas separatrix [13–16]. Another school of thought focuses on dynamics and proposes a separate “Frenkel line” as the border between liquid-like and gas-like states [17, 18]. Still another viewpoint, specific to water, focuses on the hydrogen-bond (H-bond) network structure and its related percolation

threshold [19, 20]. Meanwhile, the uniqueness of such boundaries has also been called into question [21].

In this study, we elucidate the liquid-like to gas-like crossover in supercritical water by investigating Ångström-scale dynamics *via* inelastic X-ray scattering (IXS) and molecular dynamics (MD) simulations. This choice is partly motivated by previous studies of water [22–24] and the suggestion that the presence of positive sound dispersion (PSD, the presence of an acoustic mode that disperses more quickly than in the long-wavelength, hydrodynamic limit) can be considered an indication of liquid-like behavior in the supercritical region [14, 17]. Our work determines spectral features of the dynamical response which we associate with liquid-like and gas-like behavior, and we show that there is a dramatic change in the ratio of these components around the Widom line. We also investigate the relation of these features to the dielectric properties and hydrogen bonding, which has important implications for the modeling of solvent properties of supercritical water.

IXS measurements were carried out at BL43LXU [25] of the RIKEN SPring-8 Center in Japan. We used the Si(999) reflection with 17.8 keV incident X-rays. The resolution function was measured with a 2 mm plexiglass sample and had a full width at half maximum of approximately 3 meV for all of the 20 analyzers used in the experiment. We used diamond windows and a sample length of 1.85 mm in a pressure cell specially designed for use with supercritical water [26]. Background from the empty cell with windows was measured and subtracted, though it was negligible in the frequency range of interest. We scanned from -40 meV to 40 meV in photon energy transfer, and each scan took approximately 1.5 hrs, during which the temperature and pressure were controlled within ± 5 K and ± 10 bar.

MD simulations are carried out using the LAMMPS simulation package [27]. We use *NPT* ensembles with

* Also at Stanford University Physics Department, 382 Via Pueblo Mall, Stanford, CA 94305, USA; phsun@stanford.edu

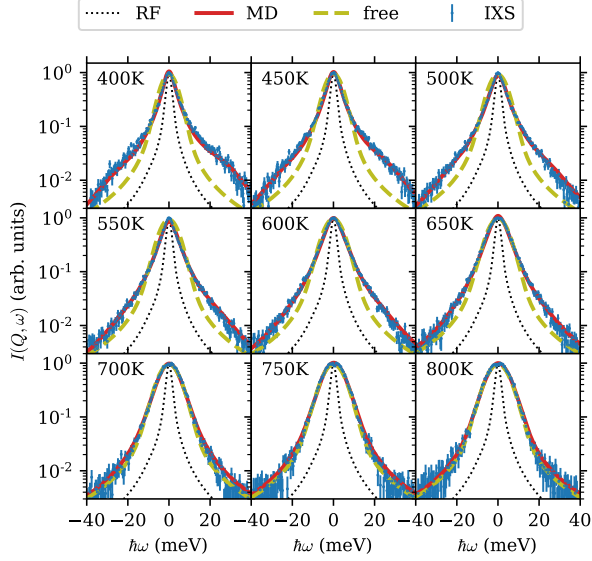


FIG. 1. Comparison of IXS data (dots with error bar) and MD simulation results (solid line) at 300 bar for $Q \approx 12 \text{ nm}^{-1}$. The MD results are multiplied by the Bose factor and convolved with the RF (dotted line). The free-gas limit (dashed line) is also plotted for comparison. All spectra are scaled to match at the center ($\omega = 0$).

2880 water molecules. After equilibration at each P - T state, the simulation is run for 1 ns at 1 fs time steps. We choose the TIP4P/2005 potential [28], which is shown to best reproduce the physical properties of water among similar models [29]; in particular, the critical temperature and density are closest to experimental values. Even though its critical pressure, $P_c^{\text{MD}} = 146 \text{ bar}$, is lower than the experimental value $P_c = 221 \text{ bar}$ by 75 bar, it is found that the TIP4P/2005 model can reproduce many dynamic and thermodynamic properties of supercritical water with a simple pressure change [15]. Therefore, we apply a 75 bar shift in our simulations to match experimental conditions, and this shift is implied in the discussions below.

In IXS, after background subtraction, the scattered intensity at momentum transfer $\hbar Q$ and energy transfer $\hbar \omega$ is [24, 30]:

$$I(Q, \omega) = I_0 [R(\omega)] * [B(\omega) S(Q, \omega)]. \quad (1)$$

Here $*$ denotes convolution; I_0 is an overall intensity factor; $R(\omega)$ is the instrument resolution function (RF); $B(\omega)$ is the Bose factor arising from detailed balance, which for liquids is generally taken to be $B(\omega) = (\hbar \omega / k_B T) / (1 - e^{-\hbar \omega / k_B T})$ [24, 30]; $S(Q, \omega)$, the *classical* dynamic structure factor, is the main quantity we are concerned with. Because the IXS signal is dominated by scattering from oxygen atoms, we include only oxygen atoms when calculating $S(Q, \omega)$ from the MD trajectories.

For ease of discussion, we first focus on the isobar $P = 300 \text{ bar}$ (225 bar for MD). Figure 1 presents a comparison

between the measured IXS spectra and MD simulation results calculated from Eq. (1). Features in the IXS data are well reproduced by the MD model. In particular, at 400 K, both MD and IXS results show clear side bumps around $\pm 25 \text{ meV}$. At $Q = 12 \text{ nm}^{-1}$, they correspond to a sound speed of approximately 3 km/s, almost twice as fast as the ultrasonic value 1.57 km/s. This is similar to what has been measured before in ambient water [22, 23] and hence suggests liquid-like dynamics. With increasing temperature, these side bumps diminish while the central peak broadens. By 800 K, the spectrum becomes very close to the ideal-gas limit (see e.g. Section 4.3 of Ref. 31):

$$S(Q, \omega) = \frac{1}{\sqrt{2\pi} Q v_0} \exp \left[-\frac{1}{2} \left(\frac{\omega}{Q v_0} \right)^2 \right], \quad (2)$$

where $v_0 \equiv \sqrt{k_B T / M}$ is the thermal velocity and M the molecular mass of water.

To better investigate this liquid-like to gas-like transition in the dynamics, we focus on the longitudinal current-current correlation function $J_l(Q, \omega)$, which is often used to investigate acoustic modes at finite wavelengths. It can be shown that $J_l(Q, \omega)$ bears a simple relation to $S(Q, \omega)$ [31]:

$$J_l(Q, \omega) = \frac{\omega^2}{Q^2} S(Q, \omega). \quad (3)$$

Moreover, because of the sum rule [31] $\int_{-\infty}^{\infty} J_l(Q, \omega) d\omega = k_B T / M$, $J_l(Q, \omega)$ can be conveniently normalized with a factor $M / k_B T$, making it easy to quantify spectral components as will be shown below. The normalized J_l spectra are presented in Fig. 2. The MD spectra are multiplied by the Bose factor which reproduces the enhanced IXS signal on the Stokes ($\omega > 0$) side. To obtain J_l from IXS data, we multiply the IXS intensities by ω^2 / Q^2 and subtract the quasi-elastic background which becomes significant near the critical point (see Appendix B). Again, details of the temperature evolution in the IXS data are well reproduced in the MD results.

Upon closer examination, two distinct components can be seen in J_l at $Q = 11 \text{ nm}^{-1}$ and 16 nm^{-1} : a low frequency (LF) component peaked below 10 meV, and a high frequency (HF) component peaked around 25 meV. While the HF component corresponds to the side bumps at lower temperatures in Fig. 1, thus representing liquid-like dynamics, the LF component eventually becomes the ideal-gas-like spectrum at high temperatures. With increasing temperature, the spectral weight shifts from HF to LF, leading to a crossover from liquid-like to gas-like dynamics. At $Q = 6 \text{ nm}^{-1}$, even though there is only one distinct peak in J_l , one may still interpret the spectra as containing two components, a HF one decreasing with temperature and a LF one increasing, with an almost isosbestic point around 8 meV.

Having established the phenomenology for the dynamic crossover, we now quantify this transition and find its physical origin. To our knowledge, however, no theory to date can be used to fully reproduce the spectra

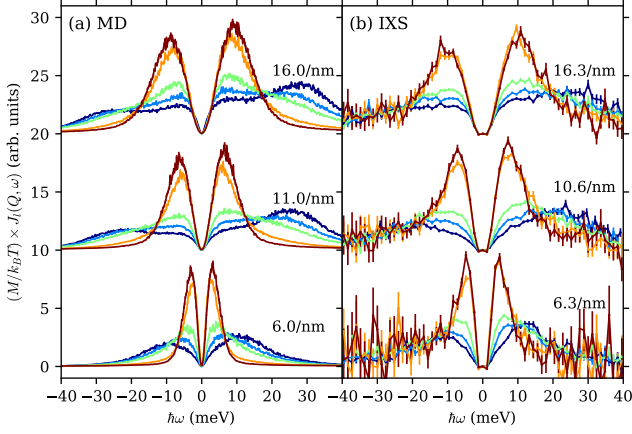


FIG. 2. Longitudinal current correlation function, $J_l(Q, \omega)$, for $P = 300$ bar obtained from (a) MD and (b) IXS. MD spectra are multiplied by the Bose factor. IXS spectra are multiplied by ω^2/Q^2 after subtracting out a scaled RF (see Appendix B). From dark blue to dark red are spectra taken from 400 K to 800 K at 100 K steps. An offset is applied between different spectra from different Q values as indicated in the plots.

shown in Fig. 2. Fitting with given spectral shapes such as damped harmonic oscillators [22, 23, 32] or the memory function [24, 33, 34], as is usually done in IXS data analyses, results in large fluctuations in the fit parameters. In addition, the physical motivation behind these fit models—the existence of acoustic modes—is lost at high temperatures when the fluid becomes gas-like. Therefore, we take a phenomenological approach and use non-negative matrix factorization (NMF), which is model-independent and has been shown to give parts-based representations of data when properly constrained [35]. Mathematically, we optimize the decomposition

$$J_l(Q, \omega; P, T) = f_{\text{HF}}(P, T) J_l^{\text{HF}}(Q, \omega) + f_{\text{LF}}(P, T) J_l^{\text{LF}}(Q, \omega) \quad (4)$$

and find the PT -independent components J_l^{HF} and J_l^{LF} , as well as their weights f_{HF} and f_{LF} for each thermodynamic state. The NNDSVD initialization [36] is used to facilitate the separation of the components, although other initializations in Ref. 36 lead to essentially the same results. Data below 6 nm^{-1} is excluded to avoid the influence from critical fluctuations (large quasi-elastic scattering intensities as seen in, e.g., Ref. 34). The data in the Q range 6 nm^{-1} to 18 nm^{-1} are fit simultaneously, i.e. with the same weights f_{HF} and f_{LF} , which is found to give consistent results. Moreover, because of the aforementioned sum rule for J_l , we may normalize the components J_l^{HF} and J_l^{LF} so they both have the same area as J_l . Then, $f_{\text{HF}} + f_{\text{LF}} = 1$ for each PT state, and in the following discussion we use $f \equiv f_{\text{HF}}$ to denote the fraction of the HF component. We note that this decomposition scheme is conceptually similar to the two-phase

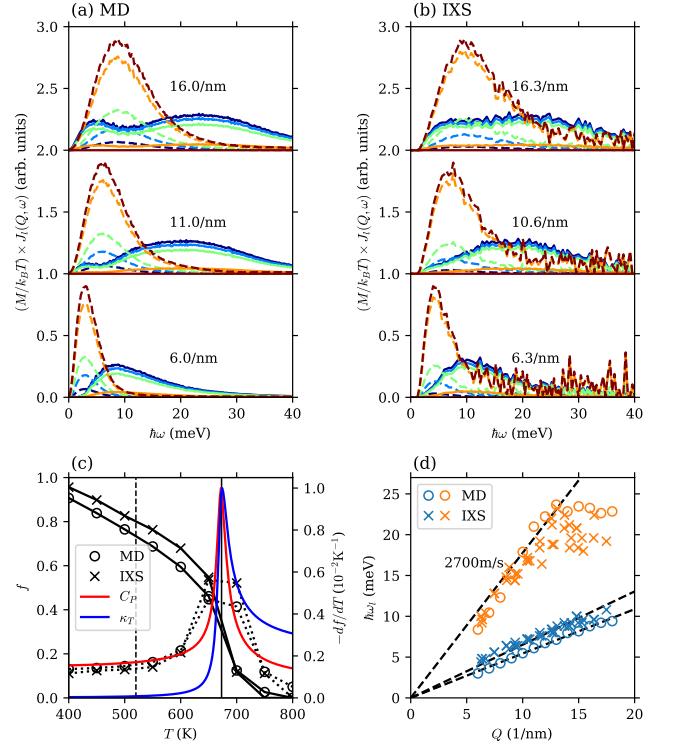


FIG. 3. NMF results. (a) Dashed and solid lines indicate the LF and HF components of the MD spectra; (b) the same for IXS spectra. Color schemes and Q values are the same as in Fig. 2. (c) Circles: MD; crosses: IXS. Black solid lines show fraction of the HF component as a function of temperature (see text), while dotted lines show their temperature derivatives; these lines are guide to the eye. Also plotted are C_P (red) and κ_T (blue) scaled to match the derivatives. Solid and dashed vertical lines indicate the approximate position of the Widom line (maximum of C_P and κ_T) and the Frenkel line [18], respectively. (d) Dispersion curves for peak frequencies of the LF (blue) and HF (orange) components. Symbols are the same as in (c); dashed lines indicate linear dispersions.

thermodynamic model proposed by Lin et al. [37, 38] and the low-frequency fraction $f_{\text{LF}} = 1 - f$ is analogous to the translational “fluidicity” parameter defined therein. However, our method avoids the need to find a reference hard-spheres system and, as discussed below, the ability to examine the Q -dependence helps provide insight into the nature of the LF and HF components.

Figure 3(a) and (b) present the NMF results for the spectra shown in Fig. 2 after dividing out the Bose factor. The shapes and temperature dependence of both components are discernible. In Fig. 3(c), it can be seen that the fraction of the HF component f obtained from MD and IXS closely follow each other, and both decrease monotonically as temperature increases. The presence of the WL is visible as a sudden drop in f , i.e. a sharp decrease in the fraction of liquid-like dynamics, as temperature rises. This becomes clearer when we look at the derivative $|df/dT|$, calculated using the finite difference

approximation, and compare it with thermodynamic response functions such as isobaric heat capacity C_P and isothermal compressibility κ_T . Thus, f can be used to describe the dynamic crossover in the supercritical region and is tied closely to thermodynamic properties. We note in passing that the Frenkel line given in Ref. 18 does not appear to correlate with significant changes in the dynamics, as shown in Fig. 3(c).

Next, we seek to identify the microscopic origin of the dynamic transition. It is helpful to examine the dispersion relations $\omega_l(Q)$ for the HF and LF components, where the mode frequency ω_l is defined as the peak frequency at a given Q . The results are shown in Fig. 3(d). For the LF component, ω_l changes linearly with Q , as expected for an ideal gas (see Appendix A). The HF component, on the other hand, has a Q -dependence characteristic of acoustic modes: it disperses linearly with Q until it flattens around 12 nm^{-1} , i.e., near the boundary of the pseudo-Brillouin zone [32], which closely resembles the longitudinal acoustic branch observed in ambient liquid water [23, 39]. Notice also that the peak frequency near the zone boundary is around 25 meV (200 cm^{-1}), recalling earlier Raman and far-IR measurements in which a peak at similar position was seen [40–42]. Even though some controversy remains on the exact mechanism giving rise to this mode in these optic measurements [43], it has been unanimously described as a translational mode between H-bonded molecules [41, 43–45], and is associated with the longitudinal acoustic phonon and the O–O stretching motion [46]. Given that the current study is sensitive only to oxygen atoms, the HF component can then be associated with the O–O stretching mode between H-bonded molecules, and thus the decrease of the HF component is associated with the diminishing of the H-bond network.

To further illustrate the correlation between H-bonding and the HF component, we plot in Fig. 4(a) the parameter f against the fraction of molecules with two or more H-bonds, $f_{\text{HB} \geq 2}$, obtained from MD results. Here we use a H-bond definition common in the literature: two molecules are H-bonded if their O–O distance is less than 3.5 \AA and the $\text{O} \cdots \text{O} - \text{H}$ angle is less than 30° [47, 48]. We note that, even though different definitions result in different H-bond populations [49–51], they lead to the same conclusions (see Appendix C). As shown in Fig. 4(a), the data collapse onto a single line, indicating a strong correlation between f and the fraction of ≥ 2 -bonded molecules. Moreover, the two quantities have an almost 1:1 ratio in the probed P - T range. We interpret this as strong evidence to identify molecules giving rise to the HF component with ≥ 2 -bonded molecules which are in the body of the H-bond network, and those contributing to the LF component with monomers and singly bonded molecules in the periphery of the H-bond clusters.

We also find good linearity between f and the enthalpy H , as shown in Fig. 4(b), which is consistent with the close resemblance between $|df/dT|$ and C_P in Fig. 3(c).

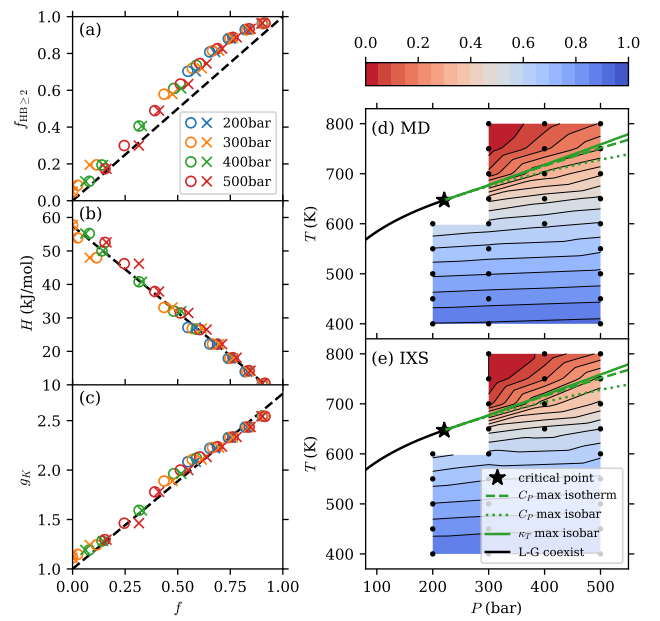


FIG. 4. Fraction of the HF component, f , plotted against (a) the fraction of molecules with two or more H-bonds, $f_{\text{HB} \geq 2}$, (b) the enthalpy H (obtained from the NIST Chemistry WebBook [52]), and (c) the Kirkwood correlation factor g_K . Circles: MD; crosses: IXS. Different colors indicate different iso-bars as shown in the legend. (d) and (e) show contour plots for f on the water phase diagram from MD and IXS, respectively. Black dots indicate states where data is taken; the contour plot is made by linear interpolation on these data. Also plotted are the critical point (black star), liquid-gas coexistence line (black line), and Widom lines by various definitions (green lines; see legend). Thermodynamic data is obtained from the IAPWS-95 equation of state [53].

The slope of the line indicates that LF and HF have an average energy difference of $\sim 52 \text{ kJ}$ per mole of molecules. This is consistent with the estimate of 23.4 kJ per mole of H-bonds [54], since molecules contributing to HF have typically two more H-bonds.

The close relation between f and H-bonding suggests that f may also be connected to chemical properties of sub- to super-critical water. Here we focus on the dielectric constant ϵ which controls the solvation behavior and is thus relevant for many chemical processes [9, 55]. Notably, ϵ decreases from around 80 under ambient conditions to about 6 near the critical point—a value close to that of organic solvents—thus able to dissolve many organic molecules [6, 9]. A widely used model for ϵ is the Kirkwood-Fröhlich equation [54–57]:

$$\frac{(\epsilon - n^2)(2\epsilon + n^2)}{\epsilon(n^2 + 2)^2} = g_K \frac{\rho \mu^2}{9M\epsilon_0 k_B T}, \quad (5)$$

where $\mu = 1.8546 \text{ D}$ is the gas-phase dipole moment of water [58] and ϵ_0 the vacuum permittivity. n is the refractive index at the reference wavelength $\lambda = 0.589 \text{ \mu m}$ [59]; we have checked that choosing $\lambda = 1.1 \text{ \mu m}$

leads to the same results. The so-called Kirkwood correlation factor, g_K , is defined as the ratio of the total dipole moment in a spherical volume surrounding a fixed molecule to the dipole moment of that molecule, in the absence of external fields. Thus, $g_K = 1$ if there is no inter-molecular correlation (as expected for a gas), and $g_K > 1$ if molecular dipoles tend to align in parallel (as in room temperature water). This definition suggests a close relation between g_K and the parameter f in our study. To investigate this, we calculate g_K using Eq. 5 and plot it against f in Fig. 4(c). Indeed, good linearity exists between these two parameters. Moreover, the data is consistent with an intercept at $g_K = 1$ for $f = 0$, where gas-like behavior is expected. Hence we show as a dashed line a linear fit fixing the intercept at $g_K = 1$. The fit indicates $g_K = 2.77$ when $f = 1$, i.e. in the absence of the LF component, which is remarkably close to the value $g_K = 2.79$ at ambient conditions (1 bar, 300 K). Therefore, we have established a close relation between f and g_K ; since the latter is tied to the dielectric constant and is suggested to influence transport properties as well [60], the parameter f can be viewed as a directly measurable quantity which characterizes chemical properties of supercritical water.

Finally, for an overview of the dynamic crossover, in Fig. 4(d) and (e) we show contour maps of f on the phase diagram. The topology is clearly influenced by the Widom line which traces the loci of highest gradients, indicating rapid shifts between liquid-like and gas-like dynamics. However, we emphasize that remnants of the HF component can be found above the Widom line and LF below, thus supporting the view of the Widom line as an indicator of continuous crossover instead of a rigid separatrix between distinct liquid-like and gas-like phases [21].

In conclusion, we have used a combination of IXS measurements and MD simulations to study the crossover from liquid-like to gas-like dynamics in supercritical water. The TIP4P/2005 model for MD well reproduces the inter-molecular dynamics measured *via* IXS. We find that the dynamics can be separated into liquid-like (HF) and gas-like (LF) components, and it is the changing ratio between the two that leads to the crossover. Through further analysis, we find a strong correlation between the fraction of the HF component and molecules with two or more H-bonds, which is significant for modeling of solvent properties such as the dielectric constant. The Widom line, which originates from thermodynamic properties, coincides with rapid changes in the inter-molecular dynamics and H-bonding as well.

ACKNOWLEDGMENTS

This work is supported by the U.S. Department of Energy, Office of Science, Office of Basic Energy Sciences under Contract No. DE-AC02-76SF00515. The synchrotron radiation experiments were performed at BL43LXU in

Spring-8 with the approval of RIKEN (Proposal No. 20180031). We would like to thank Stanford University and the Stanford Research Computing Center for providing computational resources and support that contributed to this work.

Appendix A: Molecular hydrodynamics

In this section, we define and briefly discuss the correlation functions used in our study. First, the *classical* dynamic structure factor, $S(\mathbf{Q}, \omega)$, is defined as the Fourier transform of density-density correlations:

$$S(\mathbf{Q}, \omega) \equiv \frac{1}{2\pi} \int_{-\infty}^{\infty} dt e^{-i\omega t} \langle \rho^*(\mathbf{Q}, 0) \rho(\mathbf{Q}, t) \rangle, \quad (\text{A1})$$

where $\rho(\mathbf{Q}, t)$ is the number density in momentum-space and can be written as a sum over all N atoms in the system:

$$\rho(\mathbf{Q}, t) \equiv \frac{1}{\sqrt{N}} \sum_{m=1}^N e^{i\mathbf{Q} \cdot \mathbf{r}_m(t)} \quad (\text{A2})$$

with \mathbf{r}_m being the position of the m^{th} atom.

The longitudinal current correlation function, $J_l(\mathbf{Q}, \omega)$, is defined as

$$J_l(\mathbf{Q}, \omega) \equiv \frac{1}{2\pi} \int_{-\infty}^{\infty} dt e^{-i\omega t} \langle j_l^*(\mathbf{Q}, 0) j_l(\mathbf{Q}, t) \rangle, \quad (\text{A3})$$

where

$$j_l(\mathbf{Q}, t) \equiv \frac{1}{\sqrt{N}} \sum_{m=1}^N v_{m,l}(t) e^{i\mathbf{Q} \cdot \mathbf{r}_m(t)} \quad (\text{A4})$$

is the longitudinal current density in momentum-space, and $v_{m,l}$ denotes the component of the velocity of the m^{th} particle parallel to \mathbf{Q} . Equations (A1)–(A4) are used directly in our study to calculate $S(\mathbf{Q}, \omega)$ and $J_l(\mathbf{Q}, \omega)$. In isotropic systems such as liquids, $S(\mathbf{Q}, \omega)$ and $J_l(\mathbf{Q}, \omega)$ are independent of the orientation of \mathbf{Q} . Thus we use the magnitude $Q \equiv |\mathbf{Q}|$, and in simulations we average over different \mathbf{Q} directions to reduce noise.

In the ideal-gas limit, correlations between different molecules vanish and we obtain (see e.g. Section 4.3 of Ref. 31):

$$S(Q, \omega) = \frac{1}{\sqrt{2\pi} Q v_0} \exp \left[-\frac{1}{2} \left(\frac{\omega}{Q v_0} \right)^2 \right], \quad (\text{A5})$$

where $v_0 \equiv \sqrt{k_B T / M}$ is the thermal velocity and M the molecular mass of water. $J_l(\omega, Q)$ can be obtained with $J_l(Q, \omega) = (\omega/Q)^2 S(Q, \omega)$, and its peak frequency at fixed Q is:

$$\omega_l(Q) = \sqrt{\frac{2k_B T}{M}} Q. \quad (\text{A6})$$

Appendix B: Effect of resolution function and treatment of IXS data

This section explains our procedure to obtain $J_I(Q, \omega)$ from IXS spectra. The relation $J_I(Q, \omega) = (\omega/Q)^2 S(Q, \omega)$ suggests that we simply multiply the IXS spectra by a factor $(\omega/Q)^2$. The results thus obtained are shown as solid lines in Fig. 5(c). At higher Q values 10.6 nm^{-1} and 16.3 nm^{-1} , the spectra already resemble the corresponding MD results in Fig. 5(a). For $Q = 6.3 \text{ nm}^{-1}$, however, large tails appear at higher temperatures, violating the sum rule [31] $(M/k_B T) \int_{-\infty}^{\infty} J_I(Q, \omega) d\omega = 1$. We attribute this to large quasi-elastic scattering in the dynamical structure factor $S(Q, \omega)$ arising from critical fluctuation, which in turn gives rise to IXS signal at finite ω through convolution with the resolution function (RF). Note that because of the $(\omega/Q)^2$ factor, the quasi-elastic peak ($\omega \approx 0$) should not influence the J_I spectra.

To test this hypothesis, we convolve $S(Q, \omega)$ obtained from MD with the RF and then multiply it by the factor $(\omega/Q)^2$. The results are shown in Fig. 5(b), which well reproduce the tails seen in Fig. 5(c), thus proving our hypothesis. Therefore, we account for the quasi-elastic contribution in the IXS spectra by scaling the RF to match the central part of the spectrum (-3 meV to 3 meV). These scaled RFs are shown as dashed lines in Fig. 5(c); their tails match those in the IXS spectra, again supporting the hypothesis that these tails arise from critical fluctuations. We then subtract the scaled RF from

the IXS spectra, arriving at the results in Fig. 5(d) (same as Fig. 2(b) in the main text), which appears to satisfy the sum rule and bears much resemblance to the MD results in Fig. 5(a).

Appendix C: Hydrogen bond definition

As mentioned in the main text, a variety of criteria have been used to define hydrogen-bonding (H-bonding) in water, which result in different H-bond populations [49–51]. Here we adopt the notations in Ref. 50 and 51; the variables used are defined in Fig. 6. In the main text, we use a definition commonly found in the literature [47, 48]: $R < 3.5 \text{ \AA}$ and $\beta < 30^\circ$. This criterion, henceforth referred to as the R - β definition, turns out to be a somewhat relaxed definition among all definitions [50, 51]. A relatively stringent one, introduced in Ref. 51 and denoted here as the r - ψ definition, requires

$$(7.1 - 0.050\psi + 0.00021\psi^2)e^{-r/0.343} > 0.0085, \quad (\text{C1})$$

where r is in units of Ångströms and $\psi \in [0^\circ, 90^\circ]$ in degrees.

Figure 7 presents the correlation between the parameter f defined in our work and the fraction of ≥ 2 -bonded molecules, $f_{\text{HB} \geq 2}$, based on the two definitions. Indeed, the r - ψ definition proves to be more stringent than R - β , but both show good correlation between f and $f_{\text{HB} \geq 2}$ with an almost 1:1 ratio. Therefore, our conclusion is robust against change in a range of H-bond definitions.

-
- [1] C. Cagniard de la Tour, Exposé de quelques résultats obtenus par l'action combinée de la chaleur et de la compression sur certains liquides, tels que l'eau, l'alcool, l'éther sulfurique et l'essence de pétrole rectifiée, *Annales de chimie et de physique* **21**, 127 (1822).
 - [2] B. R. T. Simoneit, Aqueous high-temperature and high-pressure organic geochemistry of hydrothermal vent systems, *Geochimica et Cosmochimica Acta* **57**, 3231 (1993).
 - [3] W. Martin, J. Baross, D. Kelley, and M. J. Russell, Hydrothermal vents and the origin of life, *Nature Reviews Microbiology* **6**, 805 (2008).
 - [4] M. Hirschmann and D. Kohlstedt, Water in Earth's mantle, *Physics Today* **65**, 40 (2012).
 - [5] T. Adschiri, Y.-W. Lee, M. Goto, and S. Takami, Green materials synthesis with supercritical water, *Green Chemistry* **13**, 1380 (2011).
 - [6] A. A. Peterson, F. Vogel, R. P. Lachance, M. Fröling, J. Antal Michael J., and J. W. Tester, Thermochemical biofuel production in hydrothermal media: A review of sub- and supercritical water technologies, *Energy & Environmental Science* **1**, 32 (2008).
 - [7] M. D. Bermejo and M. J. Cocero, Supercritical water oxidation: A technical review, *AIChE Journal* **52**, 3933 (2006).
 - [8] C. A. Eckert, B. L. Knutson, and P. G. Debenedetti, Supercritical fluids as solvents for chemical and materials processing, *Nature* **383**, 313 (1996).
 - [9] N. Akiya and P. E. Savage, Roles of water for chemical reactions in high-temperature water, *Chemical Reviews* **102**, 2725 (2002).
 - [10] A. Cunsolo, G. Pratesi, G. Ruocco, M. Sampoli, F. Sette, R. Verbeni, F. Barocchi, M. Krisch, C. Masciovecchio, and M. Nardone, Dynamics of Dense Supercritical Neon at the Transition from Hydrodynamical to Single-Particle Regimes, *Physical Review Letters* **80**, 3515 (1998).
 - [11] F. Gorelli, M. Santoro, T. Scopigno, M. Krisch, and G. Ruocco, Liquidlike behavior of supercritical fluids, *Physical Review Letters* **97**, 245702 (2006), arXiv:0611044 [cond-mat].
 - [12] L. Xu, P. Kumar, S. V. Buldyrev, S.-H. Chen, P. H. Poole, F. Sciortino, and H. E. Stanley, Relation between the Widom line and the dynamic crossover in systems with a liquid-liquid phase transition, *Proceedings of the National Academy of Sciences* **102**, 16558 (2005).
 - [13] P. F. McMillan and H. E. Stanley, Going supercritical, *Nature Physics* **6**, 479 (2010).
 - [14] G. G. Simeoni, T. Bryk, F. A. Gorelli, M. Krisch, G. Ruocco, M. Santoro, and T. Scopigno, The Widom line as the crossover between liquid-like and gas-like behaviour in supercritical fluids, *Nature Physics* **6**, 503 (2010).

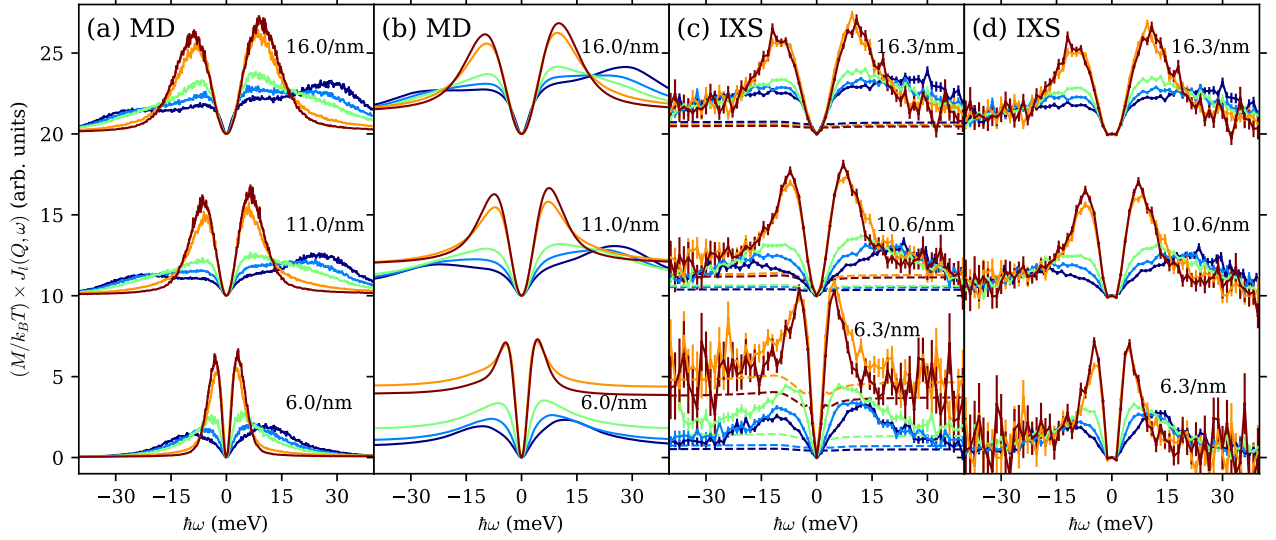


FIG. 5. Longitudinal current correlation spectra on the isobar $P = 300$ bar (225 bar for MD). Color scheme is the same as Fig. 2: from dark blue to dark red are spectra taken from 400 K to 800 K at 100 K steps. Q values are indicated as text in the plots. (a) MD spectra multiplied by the Bose factor, same as Fig. 2(a). (b) MD spectra convolved with RF. (c) Solid lines: original IXS data multiplied by $(\omega/Q)^2$; dashed lines: RF scaled to match the central part of IXS data and multiplied by $(\omega/Q)^2$. (d) IXS data with the scaled RF subtracted, same as Fig. 2(b).

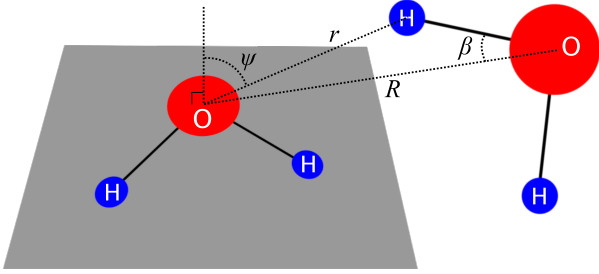


FIG. 6. Variables used in H-bond definitions (cf. Ref. 50 and 51). R : O—O distance. r : inter-molecular O—H distance. β : O...O—H angle. ψ : angle between the inter-molecular O—H vector and the normal of the acceptor molecular plane.

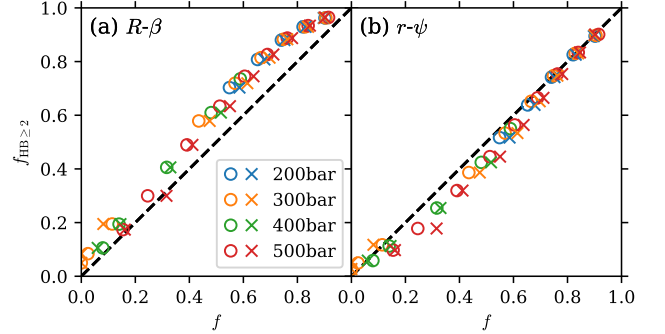


FIG. 7. Relation between f and the fraction of ≥ 2 -bonded molecules, $f_{\text{HB} \geq 2}$, based on the (a) R - β and (b) r - ψ definitions (see text). Dashed lines indicate a 1:1 ratio between f and $f_{\text{HB} \geq 2}$.

- [15] P. Gallo, D. Corradini, and M. Rovere, Widom line and dynamical crossovers as routes to understand supercritical water, *Nature Communications* **5**, 5806 (2014).
- [16] D. T. Banuti, Crossing the Widom-line Supercritical pseudo-boiling, *The Journal of Supercritical Fluids* **98**, 12 (2015).
- [17] K. Trachenko and V. V. Brazhkin, Collective modes and thermodynamics of the liquid state, *Reports on Progress in Physics* **79**, 016502 (2016), arXiv:1512.06592.
- [18] C. Yang, V. V. Brazhkin, M. T. Dove, and K. Trachenko, Frenkel line and solubility maximum in supercritical fluids, *Physical Review E* **91**, 012112 (2015), arXiv:1502.07910.
- [19] L. Pártay and P. Jedlovsky, Line of percolation in supercritical water, *The Journal of Chemical Physics* **123**, 24502 (2005).
- [20] M. Bernabei, A. Botti, F. Bruni, M. A. Ricci, and A. K. Soper, Percolation and three-dimensional structure of supercritical water, *Physical Review E* **78**, 21505 (2008).
- [21] P. Schienbein and D. Marx, Investigation concerning the uniqueness of separatrix lines separating liquidlike from gaslike regimes deep in the supercritical phase of water with a focus on Widom line concepts, *Physical Review E* **98**, 022104 (2018).
- [22] J. Teixeira, M. C. Bellissent-Funel, S. H. Chen, and B. Dorner, Observation of new short-wavelength collective excitations in heavy water by coherent inelastic neutron scattering, *Physical Review Letters* **54**, 2681 (1985).
- [23] F. Sette, G. Ruocco, M. Krisch, U. Bergmann, C. Masciovecchio, V. Mazzacurati, G. Signorelli, and R. Verbeni,

- Collective Dynamics in Water by High Energy Resolution Inelastic X-Ray Scattering, *Physical Review Letters* **75**, 850 (1995).
- [24] G. Monaco, A. Cunsolo, G. Ruocco, and F. Sette, Viscoelastic behavior of water in the terahertz-frequency range: An inelastic x-ray scattering study, *Physical Review E* **60**, 5505 (1999).
 - [25] A. Q. R. Baron, The RIKEN Quantum NanoDynamics Beamline (BL43LXU): The Next Generation for Inelastic X-Ray Scattering, *SPRING-8 Information Newsletter* **15**, 14 (2010).
 - [26] D. Ishikawa, Y. Q. Cai, D. M. Shaw, J. S. Tse, N. Hiraoaka, and A. Q. R. Baron, X-ray raman scattering of water near the critical point: Comparison of an isotherm and isochore (2012), arXiv:1210.4274.
 - [27] S. Plimpton, Fast Parallel Algorithms for Short-Range Molecular Dynamics, *Journal of Computational Physics* **117**, 1 (1995).
 - [28] J. L. F. Abascal and C. Vega, A general purpose model for the condensed phases of water: TIP4P/2005, *The Journal of Chemical Physics* **123**, 234505 (2005).
 - [29] C. Vega and J. L. F. Abascal, Simulating water with rigid non-polarizable models: a general perspective, *Physical Chemistry Chemical Physics* **13**, 19663 (2011).
 - [30] A. Q. R. Baron, High-Resolution Inelastic X-Ray Scattering Part II: Scattering Theory, Harmonic Phonons, and Calculations, in *Synchrotron Light Sources and Free-Electron Lasers*, edited by E. J. Jaeschke, S. Khan, J. R. Schneider, and J. B. Hastings (Springer International Publishing, Cham, 2020) 2nd ed., pp. 2213–2250, see also arXiv:1504.01098.
 - [31] J. P. Boon and S. Yip, *Molecular Hydrodynamics* (Dover Publications, New York, 1991).
 - [32] V. M. Giordano and G. Monaco, Fingerprints of order and disorder on the high-frequency dynamics of liquids, *Proceedings of the National Academy of Sciences* **107**, 21985 (2010).
 - [33] T. Yamaguchi, K. Yoshida, N. Yamamoto, S. Hosokawa, M. Inui, A. Q. R. Baron, and S. Tsutsui, Collective dynamics of supercritical water, *Journal of Physics and Chemistry of Solids* **66**, 2246 (2005).
 - [34] F. Bencivenga, A. Cunsolo, M. Krisch, G. Monaco, G. Ruocco, and F. Sette, High-frequency dynamics of liquid and supercritical water, *Physical Review E* **75**, 051202 (2007).
 - [35] P. O. Hoyer, Non-negative matrix factorization with sparseness constraints, *Journal of Machine Learning Research* **5**, 1457 (2004), arXiv:0408058 [cs].
 - [36] C. Boutsidis and E. Gallopoulos, SVD based initialization: A head start for nonnegative matrix factorization, *Pattern Recognition* **41**, 1350 (2008).
 - [37] S.-T. Lin, M. Blanco, and W. A. Goddard, The two-phase model for calculating thermodynamic properties of liquids from molecular dynamics: Validation for the phase diagram of Lennard-Jones fluids, *The Journal of Chemical Physics* **119**, 11792 (2003).
 - [38] S.-T. Lin, P. K. Maiti, and W. A. Goddard, Two-Phase Thermodynamic Model for Efficient and Accurate Absolute Entropy of Water from Molecular Dynamics Simulations, *The Journal of Physical Chemistry B* **114**, 8191 (2010).
 - [39] M. Sampoli, G. Ruocco, and F. Sette, Mixing of Longitudinal and Transverse Dynamics in Liquid Water, *Physical Review Letters* **79**, 1678 (1997).
 - [40] G. E. Walrafen, M. R. Fisher, M. S. Hokmabadi, and W. Yang, Temperature dependence of the low and high-frequency Raman scattering from liquid water, *The Journal of Chemical Physics* **85**, 6970 (1986).
 - [41] G. E. Walrafen, Y. C. Chu, and G. J. Piermarini, Low-Frequency Raman Scattering from Water at High Pressures and High Temperatures, *The Journal of Physical Chemistry* **100**, 10363 (1996).
 - [42] H. R. Zelsmann, Temperature dependence of the optical constants for liquid H₂O and D₂O in the far IR region, *Journal of Molecular Structure* **350**, 95 (1995).
 - [43] M. Sharma, R. Resta, and R. Car, Intermolecular Dynamical Charge Fluctuations in Water: A Signature of the H-Bond Network, *Physical Review Letters* **95**, 187401 (2005).
 - [44] W. Chen, M. Sharma, R. Resta, G. Galli, and R. Car, Role of dipolar correlations in the infrared spectra of water and ice, *Physical Review B* **77**, 245114 (2008).
 - [45] G. M. Sommers, M. F. Calegari Andrade, L. Zhang, H. Wang, and R. Car, Raman spectrum and polarizability of liquid water from deep neural networks, *Physical Chemistry Chemical Physics* **22**, 10592 (2020).
 - [46] O. F. Nielsen, Chapter 3. Low-frequency spectroscopic studies and intermolecular vibrational energy transfer in liquids, *Annual Reports Section "C"* (Physical Chemistry) **93**, 57 (1996).
 - [47] A. Luzar and D. Chandler, Hydrogen-bond kinetics in liquid water, *Nature* **379**, 55 (1996).
 - [48] A. Luzar and D. Chandler, Effect of Environment on Hydrogen Bond Dynamics in Liquid Water, *Physical Review Letters* **76**, 928 (1996).
 - [49] M. Matsumoto, Relevance of hydrogen bond definitions in liquid water, *The Journal of Chemical Physics* **126**, 54503 (2007).
 - [50] S. E. Strong, L. Shi, and J. L. Skinner, Percolation in supercritical water: Do the Widom and percolation lines coincide?, *The Journal of Chemical Physics* **149**, 84504 (2018).
 - [51] R. Kumar, J. R. Schmidt, and J. L. Skinner, Hydrogen bonding definitions and dynamics in liquid water, *The Journal of Chemical Physics* **126**, 204107 (2007).
 - [52] E. W. Lemmon, M. O. McLinden, and D. G. Friend, Thermophysical Properties of Fluid Systems, in *NIST Chemistry WebBook, NIST Standard Reference Database Number 69*, edited by P. J. Linstrom and W. G. Mallard (National Institute of Standards and Technology, Gaithersburg MD, 20899, retrieved June 8, 2020).
 - [53] W. Wagner and A. Pr  , The IAPWS Formulation 1995 for the Thermodynamic Properties of Ordinary Water Substance for General and Scientific Use, *Journal of Physical and Chemical Reference Data* **31**, 387 (2002).
 - [54] S. J. Suresh and V. M. Naik, Hydrogen bond thermodynamic properties of water from dielectric constant data, *Journal of Chemical Physics* **113**, 9727 (2000).
 - [55] H. Weing  rtner and E. U. Franck, Supercritical Water as a Solvent, *Angewandte Chemie International Edition* **44**, 2672 (2005).
 - [56] J. G. Kirkwood, The dielectric polarization of polar liquids, *The Journal of Chemical Physics* **7**, 911 (1939).
 - [57] H. Fr  hlich, *Theory of dielectrics: dielectric constant and dielectric loss*, Monographs on the physics and chemistry of materials (Clarendon Press, Oxford, 1949).
 - [58] D. R. Lide, Dielectric constants, in *CRC Handbook of Chemistry and Physics*, edited by J. R. Rumble (CRC

- Press/Taylor & Francis, Boca Raton, FL, 2019) 100th ed.
- [59] International Association for the Properties of Water and Steam, Release on the refractive index of ordinary water substance as a function of wavelength, temperature and pressure (1997).
- [60] Y. Marcus, On transport properties of hot liquid and supercritical water and their relationship to the hydrogen bonding, *Fluid Phase Equilibria* **164**, 131 (1999).